Check for updates

How to cite:
International Edition: doi.org/10.1002/anie.202201007
German Edition: doi.org/10.1002/ange.202201007

Metal–Air Batteries

Theory-Guided Regulation of FeN_4 Spin State by Neighboring Cu Atoms for Enhanced Oxygen Reduction Electrocatalysis in Flexible Metal–Air Batteries

Ting He+, Yang Chen+, Qiming Liu, Bingzhang Lu, Xianwen Song, Hongtao Liu, Min Liu, You-Nian Liu, Yi Zhang, Xiaoping Ouyang,* and Shaowei Chen**

Abstract: Iron, nitrogen-codoped carbon (Fe–N–C) nanocomposites have emerged as viable electrocatalysts for the oxygen reduction reaction (ORR) due to the formation of FeN_xC_y coordination moieties. In this study, results from first-principles calculations show a nearly linear correlation of the energy barriers of key reaction steps with the Fe magnetic moment. Experimentally, when single Cu sites are incorporated into Fe–N–C aerogels (denoted as NCAG/Fe–Cu), the Fe centers exhibit a reduced magnetic moment and markedly enhanced ORR activity within a wide pH range of 0–14. With the NCAG/Fe–Cu nanocomposites used as the cathode catalyst in a neutral/quasi-solid aluminum–air and alkaline/quasi-solid zinc–air battery, both achieve a remarkable performance with an ultrahigh open-circuit voltage of 2.00 and 1.51 V, large power density of 130 and 186 $mW\,cm^{-2}$, and good mechanical flexibility, all markedly better than those with commercial Pt/C or Pt/C-RuO_2 catalysts at the cathode.

Introduction

Among the non-precious metal electrocatalysts for the oxygen reduction reaction (ORR), transition metal and nitrogen codoped carbon (M–N–C) nanocomposites have emerged as viable candidates, mainly because of the formation of MN_xC_y moieties that possess unoccupied orbitals and can readily accommodate electron donation from oxygen intermediates.[1–5] Thus far, tremendous progress has been made in the structural engineering of the active sites and enhancement of the intrinsic activity of the M–N–C composites by, for instance, manipulation of the metal center, coordination configuration, morphological distortion, atomic vacancy, and edge defect.[6–14] Among these, Fe–N–C composites with FeN_xC_y moieties have been attracting particular attention, due to its moderate adsorption energy towards key oxygen intermediates and hence remarkable ORR activity.[15–21] Recently, it has been found that the electron spin states of the Fe centers are closely related to the catalytic activity and stability.[22–30] For instance, Bin et al.[22] proposed a spin-crossover mechanism to account for the ORR activity of Fe–N–C single-atom catalysts; Frédéric et al.[31] observed that low-/intermediate-spin FeN_xC_y moiety exhibited much enhanced durability as compared to the high-spin counterparts. Mu et al.[1] proposed that the single d_{z^2} electrons of medium-spin Fe^{III} in FeN_xC_y could readily penetrate the antibonding π-orbital of oxygen, leading to a high ORR activity. In another study,[32] first-principles calculations show that the ORR catalytic activity of MN_4 single atom sites ($M = Fe$, Co, and Ni) decreases with the decreasing magnetic moment of the metal centers (1.86, 0.62, and 0 μB, respectively). Yet, the exact correlation between the magnetic moment of the active site and the ORR activity has remained inadequately understood,[33] which impedes the rational design of high-performance ORR catalysts.

Previous studies[6,8,10,18,34] have suggested that the rate-determining step (RDS) of ORR on single Fe atom sites is the last step, the desorption of –OH, and hence the desorption energy of –OH (ΔG_{OH*}) can be used as an indicator of the ORR activity. An immediate question arises. Can ΔG_{OH*} be manipulated by the magnetic moment of the metal sites? In the present study, theoretical

---

[*] Dr. T. He,+ Y. Chen,+ X. Song, Prof. H. Liu, Prof. Y.-N. Liu, Prof. Y. Zhang
Hunan Provincial Key Laboratory of Micro & Nano Materials Interface Science, College of Chemistry and Chemical Engineering, Central South University
932 Lushan South Road, Changsha, Hunan 410083 (China)
E-mail: yzhangcsu@csu.edu.cn

Dr. T. He,+ Prof. X. Ouyang
School of Materials Science and Engineering, Xiangtan University
Yuhu District, Xiangtan, Hunan 411105 (China)
E-mail: oyxp2003@aliyun.com

Q. Liu0000-0001-5839-5453, Dr. B. Lu, Prof. S. Chen
Department of Chemistry and Biochemistry, University of California
1156 High Street, Santa Cruz, CA 95064 (USA)
E-mail: shaowei@ucsc.edu
Homepage: 0000-0001-5839-5453

Prof. M. Liu
School of Physics and Electronics, Central South University
Changsha, Hunan 410083 (China)

Prof. Y. Zhang
Key Laboratory of Materials Processing and Mold, Ministry of Education, Zhengzhou University, Zhengzhou, Henan 450002 (China)

[+] These authors contributed equally to this work.

© 2022 Wiley-VCH GmbH

calculations based on density functional theory (DFT) show that the FeN_4 site situated at different positions on a graphite sheet (e.g., basal plane, pore edge) possesses a different magnetic moment and ΔG_{OH*}, which feature a roughly linear correlation, suggesting that the ORR activity can indeed be optimized by regulating the spin state of the metal center. Experimentally, this is achieved by the introduction of single Cu atoms adjacent to the Fe centers in the Fe–N–C nanocomposites (denoted as NCAG/Fe–Cu), which exhibit a reduced magnetic moment and concurrently enhanced ORR activity within a wide pH range (0 to 14). Remarkably, the optimal sample exhibits a half-wave potential of +0.94 V and +0.84 V in alkaline and neutral media, respectively. With the NCAG/Fe–Cu composites as the cathode catalyst in a neutral/quasi-solid aluminum–air (Al–air) and alkaline/quasi-solid zinc–air (Zn–air) battery, both achieve an ultrahigh open-circuit voltage, large power density, as well as good mechanical flexibility, a performance markedly better than that with commercial Pt/C or Pt/C-RuO_2 as the cathode catalyst. Results from this study offer a new paradigm in the regulation and optimization of the electrocatalytic activity of M–N–C composites for electrochemical energy technologies.

Results and Discussion

Theoretical Computation

Generally, single metal atoms are more likely captured by graphitic carbon with rich nanopores due to abundant defects by heteroatom doping.[8,16,35–38] In the present study, three structures of the FeN_4 sites are considered computationally that are situated at different locations of a graphene sheet (details in the Supporting Information), on the basal plane (Fe_1-1, panel (i) in Figure 1a), at the nanopore edge (Fe_1-2, panel (ii) in Figure 1a), and adjacent to the nanopore (Fe_1-3, Figure S1). From the corresponding free energy diagrams of ORR at +0.90 V (vs. reversible hydrogen electrode, RHE) in Figure 1b, one can see that the RDS is

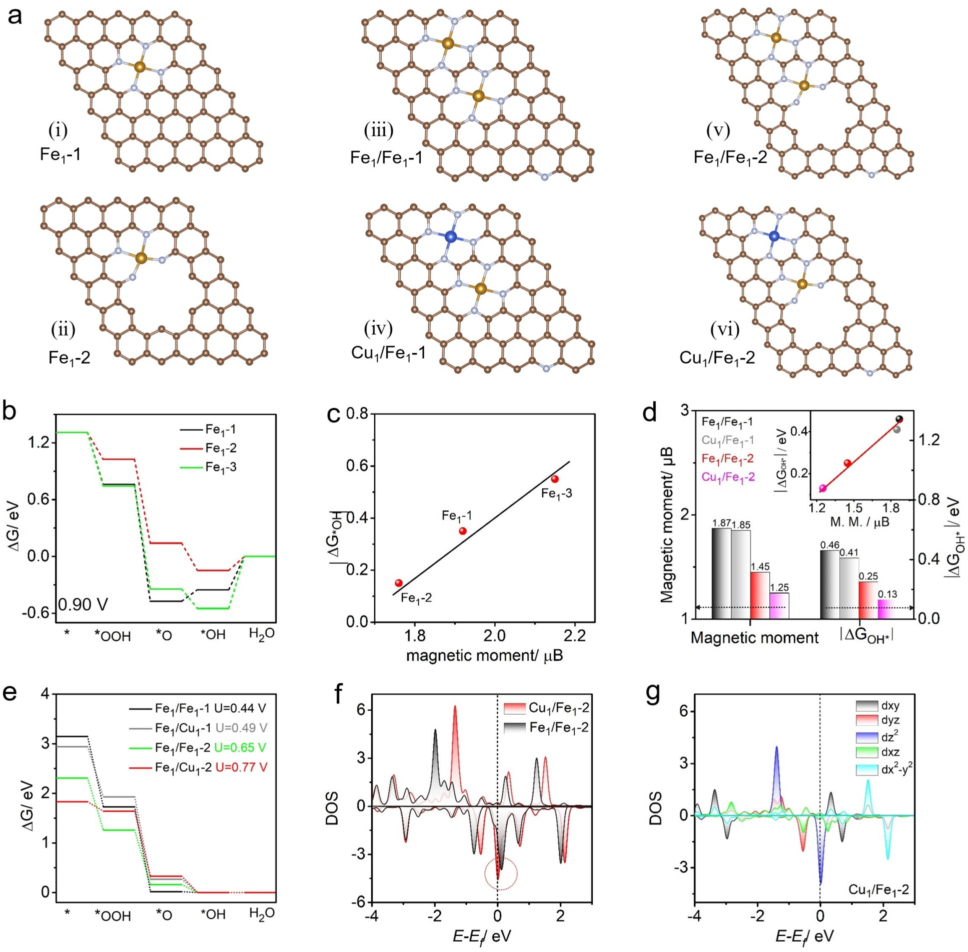

Figure 1. a) Optimal configurations of single FeN_4 sites (i) in the basal plane (Fe_1-1) and (ii) at the nanopore (Fe_1-2), and adjacent bimetal sites of (iii) Fe_1/Fe_1-1, (iv) Cu_1/Fe_1-1, (v) Fe_1/Fe_1-2 and (vi) Cu_1/Fe_1-2. b) Free energy diagrams of the Fe_1-1, Fe_1-2 and Fe_1-3 sites at +0.90 V vs. RHE. C) Correlation between magnetic moment and ΔG_{OH*} on the Fe_1-1, Fe_1-2 and Fe_1-3 sites. D) Comparison of magnetic moment and ΔG_{OH*}, inset: their correlation for Fe_1/Fe_1-1, Cu_1/Fe_1-1, Fe_1/Fe_1-2 and Cu_1/Fe_1-2. E) Free energy diagrams of the Fe_1/Fe_1-1, Cu_1/Fe_1-1, Fe_1/Fe_1-2 and Cu_1/Fe_1-2 sites at their respective limiting potentials. F) Fe 3d DOS of Fe_1/Fe_1-2 and Cu_1/Fe_1-2. G) DOS of the five Fe 3d orbitals in Cu_1/Fe_1-2.

© 2022 Wiley-VCH GmbH

the same on these various Fe sites, which is the last step of ORR, the desorption of –OH (Figure S2–S4), in good agreement with results from earlier studies.[6,8,10,18,34] Notably, results from DFT calculations show that the Fe magnetic moment exhibits a positive, quasi-linear correlation with ΔG_{OH*}, the RDS energy barrier (Figure 1c), in the order of Fe_1-2 (1.76 μB, 0.15 eV) < Fe_1-1 (1.92 μB, 0.35 eV) < Fe_1-3 (2.15 μB, 0.55 eV). That is, the FeN_4 sites at the nanopore edge (Fe_1-2) represent the preferred structure for ORR electrocatalysis.[33,39,40]

Interestingly, when a second metal site is added adjacent to FeN_4, the magnetic moment and ΔG_{OH*} can both be further manipulated. Four representative configurations are examined here. The first two involve the addition of a basal FeN_4 moiety next to Fe_1-1 and Fe_1-2, producing a homonuclear dual-metal site of Fe_1/Fe_1-1 in panel (iii) and Fe_1/Fe_1-2 in panel (v); and the second pair entails the incorporation of a basal CuN_4 moiety to Fe_1-1 and Fe_1-2, forming a heteronuclear dual-metal site of Cu_1/Fe_1-1 in panel (iv) and Cu_1/Fe_1-2 in panel (vi)—the latter were inspired by the active site structure of cytochrome c oxidase, a biological heme/copper terminal oxidase in nature.[41]

It should be noted that in these dual-metal configurations (i.e., Cu_1/Fe_1 and Fe_1/Fe_1, Figure 1a), the two metal centers are not in direct bonding interactions, and the internuclear separation (ca. 5.0 Å) is almost twice that (ca. 2.5 Å) observed when other 3d transition metals (e.g., M = Mn, Co, and Ni) are paired with Fe where direct M–Fe metal-metal bonds are generally formed.[1,37,40,42,43] This suggests minimal contributions of metal-metal charge transfer (MMCT) and orbital hybridization to the electrocatalytic activity by the Fe–Cu dual-metal structures, as such effects decay exponentially with distance.[41] It is within this context that the Cu_1/Fe_1 structures were selected to examine the correlation between the magnet moment and electrocatalytic activity of the Fe centers.

In comparison to the mononuclear system of Fe_1-1, Fe_1-2 and Fe_1-3, there are at least four observations that warrant special attention. First, these dual-metal sites also exhibit a positive, quasi-linear correlation between the magnetic moment and ΔG_{OH*} (Figure 1d and inset, and Figure S5–S9),[33,39,40] in the order of Cu_1/Fe_1-2 (1.25 μB, 0.13 eV) < Fe_1/Fe_1-2 (1.45 μB, 0.25 eV) < Cu_1/Fe_1-1 (1.85 μB, 0.41 eV) < Fe_1/Fe_1-1 (1.87 μB, 0.46 eV). Second, the incorporation of a basal CuN_4 moiety leads to a more significant diminishment of both magnetic moment and ΔG_{OH*} than the addition of a basal FeN_4 moiety. Third, the impacts of the second basal CuN_4 or FeN_4 moiety are much more significant on Fe_1-2 than on Fe_1-1. Fourth, within the present experimental context, Cu_1/Fe_1-2 represents the optimal structure with a more positive limiting potential (+0.77 V) and a lower activation energy for –OH desorption (0.20 eV) than others, indicating that it is both thermodynamically and kinetically favorable for ORR electrocatalysis (Figure 1e and S10).[44,45]

Further insights can be obtained from the density of states (DOS) of the metal site 3d electrons. From the total and Fe 3d DOS plots of Fe_1/Fe_1-2 and Cu_1/Fe_1-2 (Figure 1f and S11), it can be seen that the Fe atom at the nanopore edge makes a larger contribution to the DOS near the Fermi level (marked by a red cycle) than that on the basal plane, and the marked state of Cu_1/Fe_1-2 is much closer to the Fermi level than that of Fe_1/Fe_1-2, indicating many more active electrons for reduction reaction. Furthermore, from Figure 1g and S12, one can see that the marked state is related to the d_z^2 electrons of the Fe atom. For Cu_1/Fe_1-2, the increased electron density of the d_z^2 orbital (spin down) leads to a decrease of the magnetic moment.

Results from the above theoretical calculations suggest that the Fe spin state (i.e., magnetic moment) in FeN_4 can be readily manipulated by neighboring metal sites through the 3d electrons. This unique electronic interaction is anticipated to exert significant influence on the catalytic activity towards ORR, and the impacts are much stronger for metal sites at the nanopore edge than when the metal sites are situated on the basal plane. This is indeed confirmed in experimental measurements, as detailed below.

Sample Synthesis and Structural Analysis

In light of the results obtained above from theoretical studies, carbon aerogels doped with Fe and/or Cu were prepared by controlled pyrolysis of a biomass hydrogel template (Figure 2a). The experimental details are included in the Supporting Information. In brief, to prepare carbon aerogels doped with Fe or Cu single atoms, a hydrogel precursor was first produced by mixing gelatin with a copper(II)/iron(II)-phenanthroline (Cu/Fe–PM) complex and SiO_2 nanoparticles, and then underwent controlled pyrolysis at 500 °C in an Ar atmosphere, followed by NaOH etching to remove the SiO_2 nanoparticles, yielding the corresponding carbon aerogels that were denoted as NCAG/Fe-500 and NCAG/Cu-500, respectively.[37]

To prepare heterodinuclear Fe,Cu-codoped carbon aerogels (NCAG/Fe–Cu), the NCAG/Cu-500 aerogels obtained above were dispersed into a gelatin containing Fe-PM complex and SiO_2 nanoparticles, and the mixture was subject to a second pyrolysis at 900 °C (97 % Ar + 3 % H_2), followed by HF etching. Homodinuclear NCAG/Fe–Fe was prepared in the same manner except that NCAG/Fe-500 was used as the starting materials instead, whereas NCAG/Cu–Cu was obtained by using Cu-PM complex in place of Fe-PM. From the scanning electron microscopy (SEM) image in Figure S13, the lyophilized hydrogel can be seen to exhibit a honeycomb-like framework with a rougher surface, whereas the obtained NCAG/Fe–Cu carbon aerogels display a porous structure without metal aggregates, but rich in pores under 15 nm, as manifested in the transmission electron microscopy (TEM) images in Figure 2b and S14. Furthermore, from the scanning transmission electron microscopy (STEM) image in Figure 2c, it can be seen that pairs of small bright spots are distributed rather evenly across the carbon aerogel, indicating the dispersion of pairs of metal atoms into the carbon matrix, with a distance of about 5.1 Å (Figure 2d and S15).[7] Electron energy loss spectroscopy (EELS) measurements show that these pairs actually consist of a Fe atom and a Cu atom (Figure 2e and inset). Consistent results were obtained in elemental map-

© 2022 Wiley-VCH GmbH

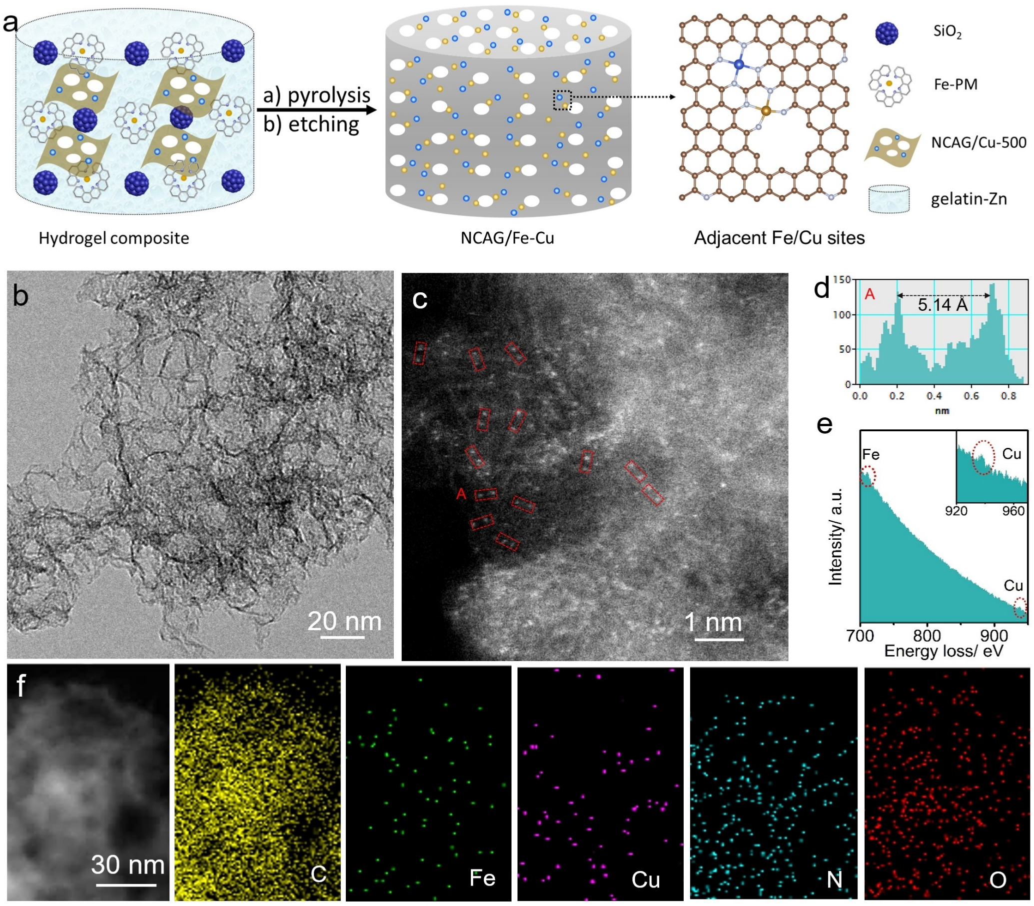

Figure 2. a) Schematic illustration of the preparation of NCAG/Fe–Cu carbon aerogels. B) TEM and c) STEM images of NCAG/Fe–Cu. D) The intensity profile and e) EELS spectrum of the red box A in (c). Inset to (e) is the zoom in of the Cu signal. f) TEM image and the corresponding elemental maps of NCAG/Fe–Cu.

ping analysis based on energy dispersive X-ray spectroscopy (EDS) which shows a uniform dispersion of the Fe and Cu atoms within the N-doped carbon scaffold (Figure 2f). Taken together, these results indicate the successful preparation of N-doped carbon aerogels embedded with Fe and Cu heteronuclear pairs.

Further structural insights of the NCAG/Fe–Cu and NCAG/Fe–Fe carbon aerogels were obtained by N_2 absorption–desorption isotherms, X-ray powder diffraction (XRD) and Raman spectroscopy measurements. Both samples can be seen to exhibit a hierarchical porous structure with an ultrahigh specific surface area over $1000\,m^2\,g^{-1}$ (Figure S16a), due to the formation of abundant nanopores, which is conducive to the capture of isolated metal sites at the nanopore edges. In fact, from the pore size distributions (Figure S16b), two major kinds of pores can be identified, nanopores/micropores (0.5 to 1 nm) and mesopores (5 to 15 nm). The corresponding XRD patterns (Figure S17a) exhibit only two broad diffraction peaks at $2\theta = 26°$ and $44°$, due to the (002) and (100) facets of graphitized carbon (PDF#41-1487), respectively. NCAG/Fe–Cu shows a slight positive shift of the (002) peak, as compared to NCAG/Fe–Fe, indicating a somewhat higher degree of graphitization. The fact that no signal of metal (oxide) species was detected is consistent with the atomic dispersion of the metal species into the carbon scaffolds. In Raman spectroscopy measurements (Figure S17b), both samples exhibit a well-defined D band at $1350.1\,cm^{-1}$ and G band at $1589.2\,cm^{-1}$, with a close D and G band intensity ratio ($I_D/I_G \approx 0.85$), indicative of a similar graphitic framework.

The elemental compositions and valence states of the carbon aerogels were then assessed by X-ray photoelectron spectroscopy (XPS) measurements. From the survey spectra in Figure S18, one can see that the NCAG/Fe–Cu and NCAG/Fe–Fe samples both contain ca. 87 wt % C, 7 wt % O, 5 wt % N, and 0.5–1 wt % metal (Table S1). The total metal contents are in good agreement with results from inductively coupled plasma-optical emission spectra (ICP-OES) analysis (Table S2), which is 0.92 wt % for NCAG/Fe–Fe, and 0.94 wt % for NCAG/Fe–Cu (0.66 wt % Fe and 0.28 wt % Cu). The high-resolution scans of the Fe 3d electrons are depicted in Figure S19, where the Fe^{II}/Fe^{III} species of NCAG/Fe–Cu can be seen to exhibit a 0.5 eV negative shift of the binding energy in comparison to those of NCAG/Fe–Fe, suggesting an increase of the Fe electron density caused by the doping of adjacent Cu atoms. From the O 1s spectra in Figure S20, deconvolution yields two

© 2022 Wiley-VCH GmbH

species, C=O at 513.2 eV and C–O/O–H at 533.3 eV, whereas no metal-O at 530.0 eV can be resolved. Yet, the metal-N (M–N) peak at 399.0 eV is obviously observed in the deconvolution of the N 1s spectra, in addition to graphitic N at 401.0 eV, and pyridinic N at 398.2 eV (Figure S21). Intriguingly, the ratio between N in metal-N and the total metal content is close to 4:1 (Table S3), suggesting that MN_4 moieties are the dominant configuration in these carbon aerogels.

X-ray absorption near-edge spectroscopy (XANES) and extended X-ray absorption fine structure (EXAFS) measurements were then performed to explore the coordination configurations of the metal sites in NCAG/Fe–Fe and NCAG/Fe–Cu. From Figure 3a, the Fe K-edge XANES profiles of both NCAG/Fe–Cu and NCAG/Fe–Fe can be seen to resemble that of iron(II) phthalocyanine (FePc), but deviate markedly from that of Fe foil, indicating a valence state somewhat under +2. Yet, the Fe K-edge in NCAG/Fe–Cu shows a slight negative shift, as compared with NCAG/Fe–Fe, suggesting a somewhat lower Fe valency, in good agreement with results from XPS measurements. In addition, the pre-edge peak at around 7113 eV, which is due to the square-planar or centrosymmetric FeN_4, shows a weaker intensity in NCAG/Fe–Cu than in NCAG/Fe–Fe and FePc, suggesting a decreasing symmetry of FeN_4 in NCAG/Fe–Cu. The R-space EXAFS profiles are depicted in Figure 3b. One can see that both the NCAG/Fe–Fe and NCAG/Fe–Cu samples display only one strong peak at about 1.4 Å, which is assigned to the Fe–N shell, similar to FePc but drastically different from Fe foil; and fitting of the Fe–N shell yields an average coordinate number of 4.0 and a bond length of ca. 2.0 Å, further confirming the formation of FeN_4 moieties (Figure S22, Table S4). From the Cu K-edge XANES profiles in Figure 3c, NCAG/Fe–Cu can be seen to show a slight positive shift in comparison to CuO, indicating a chemical state somewhat over +2. In the corresponding EXAFS profiles, a strong peak at about 1.5 Å can be observed, which is fitted to the Cu–N shell with an average coordination number of 4.0 and a bond length of 1.97 Å (Figure S23, Table S4). Taken together, these results suggest the successful production of FeN_4 and CuN_4 sites in the NCAG/Fe–Cu sample.

Further structural insights about the Fe species in NCAG/Fe–Fe and NCAG/Fe–Cu were obtained by Mössbauer and electron paramagnetic resonance (EPR) measurements. As shown in Figure 3d and e, two distinct doublets (D1 and D2) can be seen in the ^{57}Fe Mössbauer spectra of both NCAG/Fe–Fe and NCAG/Fe–Cu. D1 and D2 have comparable isomer shifts (IS) of about 0.4 mm s^{-1} but different quadrupole splitting (QS) values. Note that D1 with a mean QS value of ca. 1.0 mm s^{-1} is assigned to FeN_4 moieties in high spin, while D2 with a mean QS value of ca.

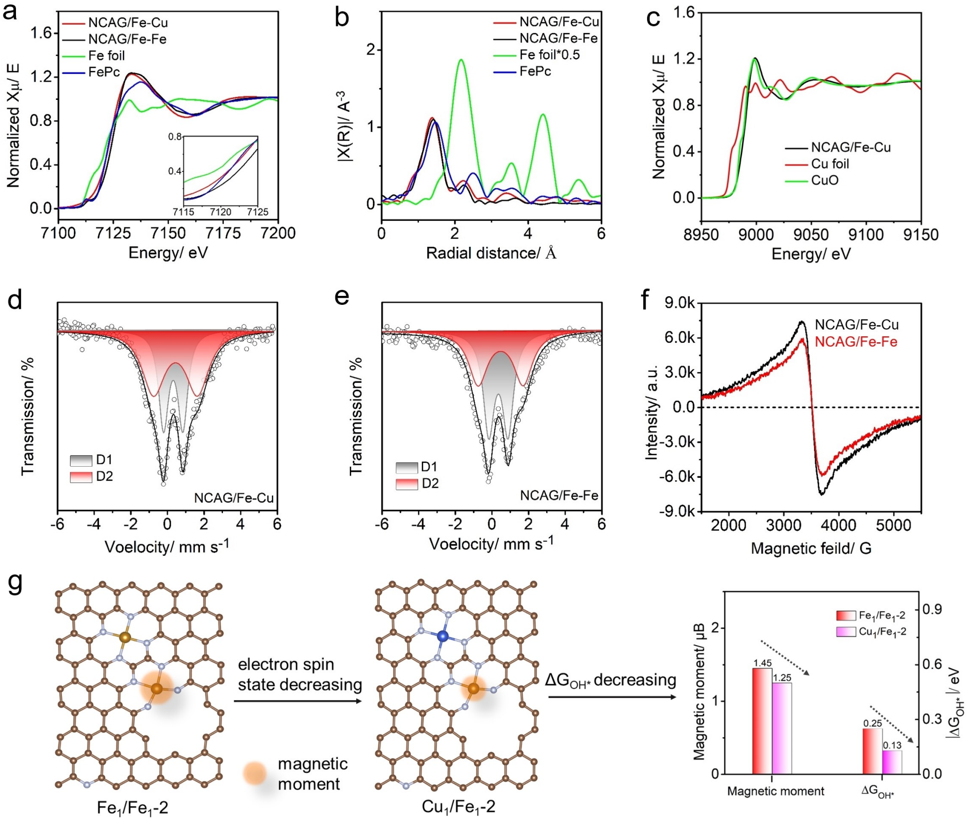

Figure 3. a) Fe K-edge XANES and b) R-space EXAFS curves of NCAG/Fe–Cu, NCAG/Fe–Fe, Fe foils and FePc. Inset to (a) is the zoom in of the absorption edge. c) Cu K-edge XANES curves of NCAG/Fe–Cu, Cu foils and CuPc. ^{57}Fe Mössbauer spectra of d) NCAG/Fe–Cu and e) NCAG/Fe. f) EPR spectra of NCAG/Fe–Cu and NCAG/Fe-Fe. g) Schematic illustration of the moderating effect of magnetic moment on ΔG_{OH*} for the bimetal sites at the nanopore.

© 2022 Wiley-VCH GmbH

2.4 mm s^{-1} is due to FeN_4 moieties in low and medium spins.[15,31] As listed in Table S5, the percentage of D2 increased from 47.7 % for NCAG/Fe–Fe to 59.8 % for NCAG/Fe–Cu, indicating a decrease of the Fe spin state after Cu doping, in good accordance with the results from theoretical calculations of the magnetic moment (Figure 1d). The increase of D2 in NCAG/Fe–Cu can also be ascribed to the inhomogeneous chemical environment in the periphery of the FeN_4 center,[46] as FeN_4 tends to reside at the nanopore edge whereas CuN_4 prefers the basal plane (Figure S24–S26). In fact, Cu_1/Fe_1-2 (panel (vi) in Figure 1a) represents an energetically favorable and stable structure.

Consistent results were obtained in EPR measurements. As compared to NCAG/Fe–Fe, NCAG/Fe–Cu shows a somewhat stronger peak in the EPR spectrum (Figure 3f).[25] This indicates lower symmetry or more defects of the FeN_4 sites, in good agreement with the formation of FeN_4 sites at the nanopore edges. Taken together, these experimental results indicate that doping of adjacent Cu atoms led to a decrease of the Fe spin state of the bimetal sites, especially those at the nanopore (e.g., Cu_1/Fe_1-2), which plays a significant role in the regulation of the electrocatalytic activity, as manifested in Figure 3g.

Electrocatalytic Activity

Remarkable ORR activity was indeed observed with the bimetal-doped carbon aerogels, which was examined by linear sweep voltammetry (LSV) measurements with a rotating disk electrode (RDE). Figure 4a shows the polarization curves of NCAG/Fe–Fe, NCAG/Fe–Cu, and commercial Pt/C (20 wt %) in O_2-saturated 0.1 M KOH. Notably, both NCAG/Fe–Cu and NCAG/Fe–Fe exhibit a superb ORR activity with an onset potential (E_{onset}) of +1.07 V and half-wave potential ($E_{1/2}$) of +0.94 V for the former and +1.04 V and +0.94 V for the latter (Figure 4b), both clearly outperforming commercial Pt/C (+0.99 V and +0.86 V) and leading transition metal-based catalysts reported recently.[47–53] Additionally, the fact that NCAG/Fe–Cu displays a 100 mV positive shift of $E_{1/2}$ as compared to NCAG/Cu–Cu (Figure S27) indicates that the Fe centers rather than the Cu ones actually act as the active sites, and the remarkably high onset and half-wave potentials of NCAG/Fe–Cu confirm the high intrinsic activity of the adjacent heteronuclear bimetal sites. Correspondingly, the NCAG/Fe–Cu sample possesses a low average H_2O_2 yield under 1.2 % within a wide potential range of +0.20 to +0.90 V (Figure S28), in comparison to NCAG/Fe–Fe and Pt/C, signifying that ORR largely followed the high-efficiency 4e^- reduction pathway. Consistent results were obtained in Koutecky–Levich analysis (Figure S29), and the kinetic current density at +0.85 V ($J_{k,0.85}$) is calculated to be as high as 25.5 mA cm^{-2} for NCAG/Fe–Cu, about twice those of NCAG/Fe–Fe (14.6 mA cm^{-2}) and Pt/C (11.2 mA cm^{-2}). In addition, the NCAG/Fe–Cu sample shows a Tafel slope of 55 mV dec^{-1}, lower than those of NCAG/Fe–Fe (60 mV dec^{-1}) and Pt/C (79 mV dec^{-1}) (Figure S30 and S31). That is, within the present experimental context, NCAG/Fe–Cu exhibits the highest kinetic current density and lowest Tafel slope, indicating the most efficient kinetics of ORR. Such a significantly enhanced ORR catalytic performance is most likely due to the doping of adjacent Cu atoms to FeN_4, in good agreement with the results from the theoretical stimulation and calculations.

The ORR activity of the heteronuclear bimetal sites was also examined in acidic and neutral media. As shown in Figure 4c, S32, and S33, NCAG/Fe–Cu also exhibits an

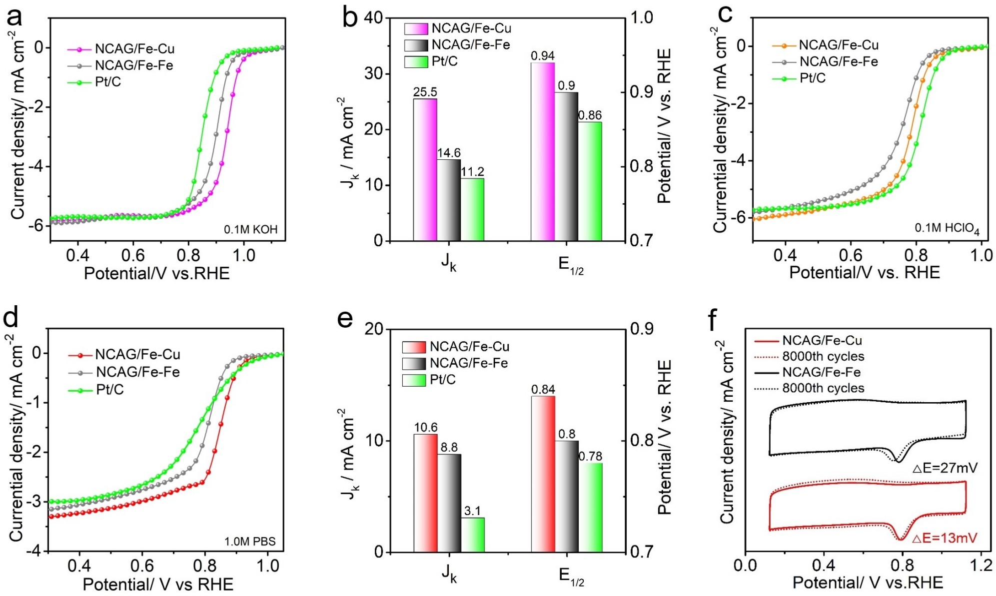

Figure 4. a) LSV curves, b) J_k (at +0.85 V) and $E_{1/2}$ of NCAG/Fe–Cu, NCAG/Fe–Fe and commercial Pt/C in 0.1 M KOH. c) LSV curves of NCAG/Fe–Cu, NCAG/Fe–Fe and commercial Pt/C in 0.1 M $HClO_4$. d) LSV curves, e) J_k (at 0.85 V) and $E_{1/2}$ of NCAG/Fe–Cu, NCAG/Fe–Fe and commercial Pt/C in 1.0 M PBS. f) CV curves of durability tests in 1.0 M PBS.

© 2022 Wiley-VCH GmbH

excellent ORR performance in 0.5 M $HClO_4$ with $E_{1/2}=+0.79$ V and a Tafel slope of 68 mV dec^{-1}, which is comparable to those of Pt/C (+0.81 V, 68 mV dec^{-1}) and better than that of NCAG/Fe–Fe (+0.76 V, 67 mV dec^{-1}). Significantly, NCAG/Fe–Cu even displays a remarkable ORR activity in neutral media (1.0 M PBS, Figure 4d and e) with an $E_{1/2}$ of 0.84 V, which is 40 mV and 60 mV more positive than those of NCAG/Fe–Fe and Pt/C, respectively, outperforming most neutral ORR catalysts reported previously.[47,54,55] Furthermore, NCAG/Fe–Cu possesses the largest $J_{k,0.85}$ of 10.6 mA cm^{-2} and lowest Tafel slope of 73 mV dec^{-1} among the series (Figure 4e and S34, S35). The low H_2O_2 yields in both acidic and neutral media of NCAG/Fe–Cu attest the high ORR efficiency (Figure S36 and S37), in accord with results from the Koutecky–Levich analysis (Figure S38).

In addition to the high ORR activity, stability is another key parameter for practical applications. This was evaluated by prolonged repetitive potential cycling. As shown in Figure 4f, the peak potential of oxygen reduction in 1.0 M PBS shifts negatively by only 13 mV after 8000 cycles with NCAG/Fe–Cu, only $^{1}/_{2}$ that observed with NCAG/Fe–Fe (27 mV). Similar results were obtained in 0.1 M KOH and 0.1 M $HClO_4$ (Figure S39). This suggests excellent stability of the nanocomposites in these different electrolyte media.

Indeed, microscopic and spectroscopic characterizations of the nanocomposite catalysts after the stability tests confirmed the structural stability of the samples. ICP-OES measurements showed virtually no change of the metal contents in both NCAG/Fe–Cu and NCAG/Fe–Fe (Table S6). In XPS measurements, the Fe 3p binding energy showed a positive shift of 0.23 eV for NCAG/Fe–Cu and 0.53 eV for NCAG/Fe–Fe, as compared to that of the as-prepared samples (Figure S40 and S41). This suggests enhanced anti-oxidation of the Fe sites in NCAG/Fe–Cu, a unique feature conducive to good stability of Fe–N–C catalysts, since the oxidized Fe species tend to escape from the carbon substrate and aggregate to form Fe_2O_3 nanoparticles.[31] In fact, the number of Fe_2O_3 nanoclusters produced after the stability tests was substantially lower in NCAG/Fe–Cu than in NCAG/Fe–Fe, as manifested in TEM and HAADF-STEM measurements (Figure S42 and S43). The enhanced stability of NCAG/Fe–Cu is likely due to the higher degree of graphitization and lower Fe valency of NCAG/Fe–Cu, as evidenced in XANES and XRD measurements (vide ante).

Taken together, through deliberate manipulation of the Fe spin state, NCAG/Fe–Cu achieved an excellent ORR performance in a wide pH range, and even outperformed commercial Pt/C in alkaline and neutral media. This is important for the practical applications under various conditions, such as alkaline/neutral metal–air batteries and proton exchange membrane fuel cells, as demonstrated below.

Applications in Solid Metal–Air Batteries

With the remarkable electrocatalytic activity towards ORR, the practical application of NCAG/Fe–Cu was then evaluated in both quasi-solid aluminum–air (Al–air) and zinc–air (Zn–air) batteries.[56,57] Note that for the alkaline/liquid Al–air battery, the battery performance and stability may be greatly discounted by the severe hydrogen evolution on the anodic Al plate in alkaline media. Fortunately, this side reaction can be markedly suppressed by using a neutral/(quasi-)solid electrolyte. However, the slower ORR kinetics in a neutral/(quasi-)solid electrolyte than in alkaline/liquid media necessitates a higher intrinsic activity of the catalysts to produce a satisfactory performance. In view of the outstanding ORR performance of NCAG/Fe–Cu in neutral media, a quasi-solid Al–air battery was assembled by using an Al plate as the anode and NCAG/Fe–Cu as the cathode catalyst, and a sodium polyacrylate (PANa) hydrogel containing a 10 wt % NaCl solution as the quasi-solid electrolyte. As shown in Figure 5a and b, the open circuit voltage and peak power density of the NCAG/Fe-Cu//Al battery is estimated to be 2.00 V and 137 mW cm^{-2}, which is about 200 mV and 41 mW cm^{-2} higher than those of a Pt/C//Al battery. Figure 5c compares the corresponding constant current discharge tests at various current densities (5, 10, 20, and 50 mA cm^{-2}) of the two batteries. One can see that the NCAG/Fe–Cu//Al battery exhibited a much higher discharge voltage within a range of current densities from 5 to 50 mA cm^{-2}, and the discharge voltage reached 1.59 V at the current density of 10 mA cm^{-2}. When the PANa hydrogel thickness was compressed by 20 %, 40 % and 60 %, the NCAG/Fe–Cu//Al battery still retained 95 %, 94 % and 92 % of the maximum power density (Figure 5b), indicating good mechanical flexibility. In addition, this NCAG/Fe–Cu//Al quasi-solid battery can produce a high open circuit voltage of 1.9 V even at a low environmental temperature of −20 °C. Apart from the excellent flexibility and low temperature tolerance, the NCAG/Fe–Cu//Al quasi-solid battery also shows a much better performance than related neutral/liquid battery (Figure 5d–f), within the context of the open circuit voltage (2.00 vs. 1.82 V), maximum power density (137 vs. 96 mW cm^{-2}) and constant current discharge voltage (1.59 V vs. 1.47 V, at 10 mA cm^{-2}).

For a rechargeable Zn–air battery, the cathode catalyst needs to display bifunctional activity toward both ORR and oxygen evolution reaction (OER). The OER activity of NCAG/Fe–Cu was then tested in 1.0 M KOH by LSV measurements, with commercial RuO_2 as the comparative benchmark. From Figure S44a, NCAG/Fe–Cu can be seen to show an overpotential (η_{10}) of 380 mV to reach the current density of 10 mA cm^{-2}, close to that of RuO_2 (376 mV). Additionally, the potential gap (ΔE) between the ORR potential at 3 mA cm^{-2} ($E_{ORR,3}$) and OER potential at 10 mA cm^{-2} ($E_{OER,10}$) is 0.67 V for NCAG/Fe–Cu, 70 mV lower than that (0.74 V) for Pt/C-RuO_2. In light of the excellent bifunctional ORR/OER performance in alkaline media of NCAG/Fe–Cu, an alkaline/quasi-solid Zn–air battery was also assembled by using NCAG/Fe–Cu (or Pt/C-RuO_2 mixture at the mass ratio of 1:1) as the cathode

© 2022 Wiley-VCH GmbH

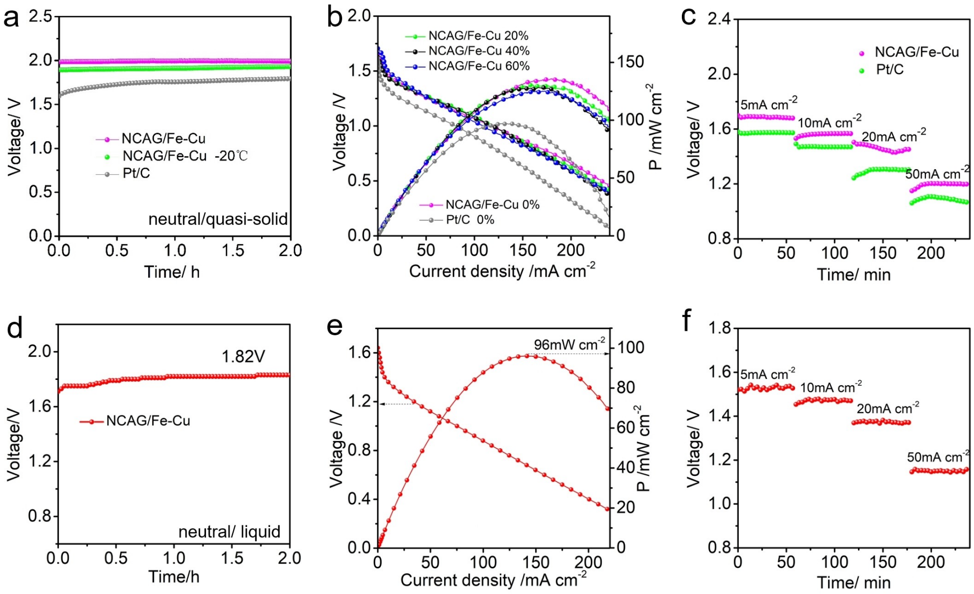

Figure 5. a) Open circuit voltages, b) discharge polarization and the corresponding power density curves at 0%, 20%, 40% and 60% compression, and c) constant current discharge tests of a neutral/quasi-solid Al–air battery with NCAG/Fe–Cu and Pt/C as the cathodic catalysts. d) Open circuit voltage, e) discharge polarization and corresponding power density curves, and f) constant current discharge tests of a neutral/liquid Al–air battery assembled with NCAG/Fe–Cu.

catalyst, a Zn plate as the anode, a PANa hydrogel containing 6 M KOH as the quasi-solid electrolyte. From Figure S44b and S44c, the NCAG/Fe–Cu//Zn quasi-solid battery can be seen to exhibit an open circuit voltage of 1.51 V and a maximum power density of 186 mW cm^{-2}, far superior to those of the Pt/C-RuO$_2$ counterpart (1.40 V and 100 mW cm^{-2}). Additionally, in comparison with Pt/C-RuO$_2$, the NCAG/Fe–Cu//Zn battery exhibited a much higher discharge voltage at the current density from 5 to 50 mA cm^{-2}, and the discharge voltage can reach 1.38 V at a current density of 5 mA cm^{-2} (Figure S44d). For the discharge–charge test (Figure S45a), NCAG/Fe–Cu//Zn battery afforded a smaller voltage gap of 0.82 V and a higher round-trip efficiency of 57% after 800 cycles, much better than those of Pt/C-RuO$_2$ (0.98 V, 49%, after 400 cycles). This performance of the NCAG/Fe–Cu//Zn battery far surpasses those of relevant solid Zn–air batteries and even liquid ones reported earlier (Table S7 and Figure S45b).[37,47,58–70]

Notably, when the PANa thickness was compressed by 30% and 60%, the solid battery still retained 95% and 93% of the maximum power and almost unchanged discharge–charge voltages (Figure S44c and S45c). In addition, when the battery was bended by 90° and 180°, the discharge voltage remained stable at 1.38 V at the current density of 5 mA cm^{-2} (Figure S45d). These compression and bending experiments indicate excellent mechanical flexibility of the NCAG/Fe–Cu battery, a unique feature for flexible electronics.

Conclusion

In summary, results from first-principles calculations showed that the Fe spin state (magnetic moment) of the FeN$_4$ moieties could be readily manipulated by the incorporation of a second, neighboring metal atom due to altering of the 3d electrons. This exerted a significant influence on the ORR catalytic activity, which was much stronger for FeN$_4$ sites situated at the nanopore edge than on the basal plane. Experimentally, a decreasing magnetic moment was indeed observed when Cu atomic sites were embedded into the NCAG/Fe–Cu aerogels, forming Fe–Cu heteronuclear pairs as attested in microscopic and spectroscopic measurements. Electrochemically, the resulting NCAG/Fe–Cu composites exhibited a remarkable ORR activity with a high half-wave potential of +0.94 V, +0.84 V and +0.78 V in alkaline, neutral and acidic media, respectively. Note that the performance in alkaline and neutral media was even better than that of commercial Pt/C, whereas the acidic performance was comparable. When the NCAG/Fe–Cu were used as the cathode catalyst in a neutral/quasi-solid Al–air or Zn–air battery, the battery achieved an ultrahigh open-circuit voltage (2.00 V, 1.51 V), large power density (130 mW cm^{-2}, 186 mA cm^{-2}), as well as good mechanical flexibility, markedly outperforming those with commercial Pt/C (or Pt/C-RuO$_2$) as the cathode catalysts. Results from this study highlight the fundamental significance of the electron spin state of metal sites in the regulation of the ORR catalytic activity, which may be exploited as a powerful strategy for the design and engineering of high-performance catalysts for electrochemical energy technologies.

© 2022 Wiley-VCH GmbH

Acknowledgements

H.T.L. acknowledged the National Key R&D Program of China (No. 2019YFA0210300). Y.Z. acknowledged support from the National Natural Science Foundation of China (21972169, 21773311) and Hunan Provincial Science and Technology Plan Project (2017TP1001). T.H. thanks the Postdoctoral Research Foundation of Central South University (140050038); Y.C. was supported by the Fundamental Research Funds for the Central Universities of Central South University (1053320210820). S.W.C. acknowledged support from the National Science Foundation (CHE-2003685 and CHE-1900235). The authors thank Eceshi (www.eceshi.com) and high-performance computing center of CSU.

Conflict of Interest

The authors declare no conflict of interest.

Data Availability Statement

The data that support the findings of this study are available from the corresponding author upon reasonable request.

Keywords: Electron Spin State · Heteronuclear Site · Magnetic Moment · Metal–Air Battery · Oxygen Reduction Reaction

---

[1] G. Yang, J. Zhu, P. Yuan, Y. Hu, G. Qu, B.-A. Lu, X. Xue, H. Yin, W. Cheng, J. Cheng, W. Xu, J. Li, J. Hu, S. Mu, J.-N. Zhang, *Nat. Commun.* **2021**, *12*, 1734.

[2] L. Li, S. Huang, R. Cao, K. Yuan, C. Lu, B. Huang, X. Tang, T. Hu, X. Zhuang, Y. Chen, *Small* **2022**, *18*, 2105387.

[3] H. Jing, P. Zhu, X. Zheng, Z. Zhang, D. Wang, Y. Li, *Adv. Powder Mater.* **2022**, *1*, 100013.

[4] M. Chen, X. Li, F. Yang, B. Li, T. Stracensky, S. Karakalos, S. Mukerjee, Q. Jia, D. Su, G. Wang, G. Wu, H. Xu, *ACS Catal.* **2020**, *10*, 10523–10534.

[5] J. Li, M. Chen, D. A. Cullen, S. Hwang, M. Wang, B. Li, K. Liu, S. Karakalos, M. Lucero, H. Zhang, C. Lei, H. Xu, G. E. Sterbinsky, Z. Feng, D. Su, K. L. More, G. Wang, Z. Wang, G. Wu, *Nat. Catal.* **2018**, *1*, 935–945.

[6] Y. Chen, S. Ji, Y. Wang, J. Dong, W. Chen, Z. Li, R. Shen, L. Zheng, Z. Zhuang, D. Wang, Y. Li, *Angew. Chem. Int. Ed.* **2017**, *56*, 6937–6941; *Angew. Chem.* **2017**, *129*, 7041–7045.

[7] D. Wang, A. Han, X. Wang, K. Tang, Z. Zhang, C. Ye, K. Kong, H. Hu, L. Zheng, P. Jiang, C. Zhao, Q. Zhang, Y. Li, *Angew. Chem. Int. Ed.* **2021**, *60*, 19262–19271; *Angew. Chem.* **2021**, *133*, 19411–19420.

[8] Y. Han, Y. Wang, W. Chen, R. Xu, L. Zheng, J. Zhang, J. Luo, R. Shen, Y. Zhu, W. Cheong, C. Chen, Q. Peng, D. Wang, Y. Li, *J. Am. Chem. Soc.* **2017**, *139*, 17269–17272.

[9] W. J. Wu, Y. Liu, D. Liu, W. X. Chen, Z. Y. Song, X. M. Wang, Y. M. Zheng, N. Lu, C. X. Wang, J. J. Mao, Y. D. Li, *Nano Res.* **2021**, *14*, 998–1003.

[10] T. He, B. Lu, Y. Chen, Y. Wang, Y. Zhang, J. L. Davenport, A. P. Chen, C.-W. Pao, M. Liu, Z. Sun, *Research* **2019**, *2019*, 6813585.

[11] K. Chen, K. Liu, P. An, H. Li, Y. Lin, J. Hu, C. Jia, J. Fu, H. Li, H. Liu, Z. Lin, W. Li, J. Li, Y.-R. Lu, T.-S. Chan, N. Zhang, M. Liu, *Nat. Commun.* **2020**, *11*, 4173.

[12] Y. Lin, K. Liu, K. Chen, Y. Xu, H. Li, J. Hu, Y.-R. Lu, T.-S. Chan, X. Qiu, J. Fu, M. Liu, *ACS Catal.* **2021**, *11*, 6304–6315.

[13] Y. Li, X. Liu, L. Zheng, J. Shang, X. Wan, R. Hu, X. Guo, S. Hong, J. Shui, *J. Mater. Chem. A* **2019**, *7*, 26147–26153.

[14] C. Xia, Y. Qiu, Y. Xia, P. Zhu, G. King, X. Zhang, Z. Wu, J. Y. Kim, D. A. Cullen, D. Zheng, P. Li, M. Shakouri, E. Heredia, P. Cui, H. N. Alshareef, Y. Hu, H. Wang, *Nat. Chem.* **2021**, *13*, 887–894.

[15] T. Mineva, I. Matanovic, P. Atanassov, M.-T. Sougrati, L. Stievano, M. Clémancey, A. Kochem, J.-M. Latour, F. Jaouen, *ACS Catal.* **2019**, *9*, 9359–9371.

[16] X. Fu, N. Li, B. Ren, G. Jiang, Y. Liu, F. M. Hassan, D. Su, J. Zhu, L. Yang, Z. Bai, Z. P. Cano, A. Yu, Z. Chen, *Adv. Energy Mater.* **2019**, *9*, 1803737.

[17] R. Ma, G. Lin, Q. Ju, W. Tang, G. Chen, Z. Chen, Q. Liu, M. Yang, Y. Lu, J. Wang, *Appl. Catal. B* **2020**, *265*, 118593.

[18] N. Zhang, T. Zhou, M. Chen, H. Feng, R. Yuan, C. a Zhong, W. Yan, Y.-C. Tian, X. Wu, W. Chu, C. Wu, Y. Xie, *Energy Environ. Sci.* **2020**, *13*, 111–118.

[19] Z. Jin, P. Li, Y. Meng, Z. Fang, D. Xiao, G. Yu, *Nat. Catal.* **2021**, *4*, 615–622.

[20] U. I. Kramm, J. Herranz, N. Larouche, T. M. Arruda, M. Lefèvre, F. Jaouen, P. Bogdanoff, S. Fiechter, I. Abs-Wurmbach, S. Mukerjee, J.-P. Dodelet, *Phys. Chem. Chem. Phys.* **2012**, *14*, 11673–11688.

[21] T. Cui, Y.-P. Wang, T. Ye, J. Wu, Z. Chen, J. Li, Y. Lei, D. Wang, Y. Li, *Angew. Chem. Int. Ed.* **2022**, *61*, e202115219; *Angew. Chem.* **2022**, *134*, e202115219.

[22] X. N. Li, C. S. Cao, S. F. Hung, Y. R. Lu, W. Z. Cai, A. I. Rykov, S. Miao, S. B. Xi, H. B. Yang, Z. H. Hu, J. H. Wang, J. Y. Zhao, E. E. Alp, W. Xu, T. S. Chan, H. M. Chen, Q. H. Xiong, H. Xiao, Y. Q. Huang, J. Li, T. Zhang, B. Liu, *Chem* **2020**, *6*, 3440–3454.

[23] U. I. Kramm, M. Lefèvre, N. Larouche, D. Schmeisser, J.-P. Dodelet, *J. Am. Chem. Soc.* **2014**, *136*, 978–985.

[24] J. Li, S. Ghoshal, W. Liang, M.-T. Sougrati, F. Jaouen, B. Halevi, S. McKinney, G. McCool, C. Ma, X. Yuan, Z.-F. Ma, S. Mukerjee, Q. Jia, *Energy Environ. Sci.* **2016**, *9*, 2418–2432.

[25] Z. Li, Z. Zhuang, F. Lv, H. Zhu, L. Zhou, M. Luo, J. Zhu, Z. Lang, S. Feng, W. Chen, L. Mai, S. Guo, *Adv. Mater.* **2018**, *30*, 1803220.

[26] W. Liu, L. Zhang, X. Liu, X. Liu, X. Yang, S. Miao, W. Wang, A. Wang, T. Zhang, *J. Am. Chem. Soc.* **2017**, *139*, 10790–10798.

[27] S. Wagner, H. Auerbach, C. E. Tait, I. Martinaiou, S. C. N. Kumar, C. Kübel, I. Sergeev, H.-C. Wille, J. Behrends, J. A. Wolny, V. Schünemann, U. I. Kramm, *Angew. Chem. Int. Ed.* **2019**, *58*, 10486–10492; *Angew. Chem.* **2019**, *131*, 10596–10602.

[28] A. Zitolo, V. Goellner, V. Armel, M.-T. Sougrati, T. Mineva, L. Stievano, E. Fonda, F. Jaouen, *Nat. Mater.* **2015**, *14*, 937–942.

[29] K. Liu, J. Fu, Y. Lin, T. Luo, G. Ni, H. Li, Z. Lin, M. Liu, *Nat. Commun.* **2022**, *13*, 2075.

[30] H. Li, S. Di, P. Niu, S. Wang, J. Wang, L. Li, *Energy Environ. Sci.* **2022**, *15*, 1601–1610.

[31] J. Li, M. T. Sougrati, A. Zitolo, J. M. Ablett, I. C. Oğuz, T. Mineva, I. Matanovic, P. Atanassov, Y. Huang, I. Zenyuk, A. Di Cicco, K. Kumar, L. Dubau, F. Maillard, G. Dražić, F. Jaouen, *Nat. Catal.* **2021**, *4*, 10–19.

[32] S. Kattel, G. Wang, *J. Mater. Chem. A* **2013**, *1*, 10790–10797.

[33] I.-Y. Jeon, S. Zhang, L. Zhang, H.-J. Choi, J.-M. Seo, Z. Xia, L. Dai, J.-B. Baek, *Adv. Mater.* **2013**, *25*, 6138–6145.

[34] B. Lu, T. J. Smart, D. Qin, J. E. Lu, N. Wang, L. Chen, Y. Peng, Y. Ping, S. Chen, *Chem. Mater.* **2017**, *29*, 5617–5628.

© 2022 Wiley-VCH GmbH

[35] M. Xiao, Z. Xing, Z. Jin, C. Liu, J. Ge, J. Zhu, Y. Wang, X. Zhao, Z. Chen, *Adv. Mater.* **2020**, *32*, 2004900.
[36] Y. Zhou, G. Chen, Q. Wang, D. Wang, X. Tao, T. Zhang, X. Feng, K. Müllen, *Adv. Funct. Mater.* **2021**, *31*, 2102420.
[37] Y. Chen, S. Hu, F. Nichols, F. Bridges, S. Kan, T. He, Y. Zhang, S. Chen, *J. Mater. Chem. A* **2020**, *8*, 11649–11655.
[38] T. He, Y. Zhang, Y. Chen, Z. Zhang, H.-Y. Wang, Y. Hu, M. Liu, C.-W. Pao, J.-L. Chen, L.-Y. Chang, Z. Sun, J. Xiang, Y. Zhang, S. Chen, *J. Mater. Chem. A* **2019**, *7*, 20840–20846.
[39] J. Miao, Y. Zhu, J. Lang, J. Zhang, S. Cheng, B. Zhou, L. Zhang, P. J. J. Alvarez, M. Long, *ACS Catal.* **2021**, *11*, 9569–9577.
[40] H. Li, J. Wang, R. Qi, Y. Hu, J. Zhang, H. Zhao, J. Zhang, Y. Zhao, *Appl. Catal. B* **2021**, *285*, 119778.
[41] C. Du, Y. Gao, H. Chen, P. Li, S. Zhu, J. Wang, Q. He, W. Chen, *J. Mater. Chem. A* **2020**, *8*, 16994–17001.
[42] Y. Wang, Z. Li, P. Zhang, Y. Pan, Y. Zhang, Q. Cai, S. R. P. Silva, J. Liu, G. Zhang, X. Sun, Z. Yan, *Nano Energy* **2021**, *87*, 106147.
[43] J. Wang, Z. Huang, W. Liu, C. Chang, H. Tang, Z. Li, W. Chen, C. Jia, T. Yao, S. Wei, Y. Wu, Y. Li, *J. Am. Chem. Soc.* **2017**, *139*, 17281–17284.
[44] Y. H. He, Q. R. Shi, W. T. Shan, X. Li, A. J. Kropf, E. C. Wegener, J. Wright, S. Karakalos, D. Su, D. A. Cullen, G. F. Wang, D. J. Myers, G. Wu, *Angew. Chem. Int. Ed.* **2021**, *60*, 9516–9526; *Angew. Chem.* **2021**, *133*, 9602–9612.
[45] J. Z. Li, H. G. Zhang, W. Samarakoon, W. T. Shan, D. A. Cullen, S. Karakalos, M. J. Chen, D. M. Gu, K. L. More, G. F. Wang, Z. X. Feng, Z. B. Wang, G. Wu, *Angew. Chem. Int. Ed.* **2019**, *58*, 18971–18980; *Angew. Chem.* **2019**, *131*, 19147–19156.
[46] U. I. Koslowski, I. Abs-Wurmbach, S. Fiechter, P. Bogdanoff, *J. Phys. Chem. C* **2008**, *112*, 15356–15366.
[47] M. Zhao, H. Liu, H. Zhang, W. Chen, H. Sun, Z. Wang, B. Zhang, L. Song, Y. Yang, C. Ma, Y. Han, W. Huang, *Energy Environ. Sci.* **2021**, *14*, 6455–6463.
[48] T. Sun, Y. Li, T. Cui, L. Xu, Y.-G. Wang, W. Chen, P. Zhang, T. Zheng, X. Fu, S. Zhang, Z. Zhang, D. Wang, Y. Li, *Nano Lett.* **2020**, *20*, 6206–6214.
[49] H. Shang, X. Zhou, J. Dong, A. Li, X. Zhao, Q. Liu, Y. Lin, J. Pei, Z. Li, Z. Jiang, D. Zhou, L. Zheng, Y. Wang, J. Zhou, Z. Yang, R. Cao, R. Sarangi, T. Sun, X. Yang, X. Zheng, W. Yan, Z. Zhuang, J. Li, W. Chen, D. Wang, J. Zhang, Y. Li, *Nat. Commun.* **2020**, *11*, 3049.
[50] L. Yan, L. Xie, X.-L. Wu, M. Qian, J. Chen, Y. Zhong, Y. Hu, *Carbon Energy* **2021**, *3*, 856–865.
[51] D. Wang, Y. Wu, Z. Li, H. Pan, Y. Wang, M. Yang, G. Zhang, *Chem. Eng. J.* **2021**, *424*, 130401.
[52] W. Wan, Y. Zhao, S. Wei, C. A. Triana, J. Li, A. Arcifa, C. S. Allen, R. Cao, G. R. Patzke, *Nat. Commun.* **2021**, *12*, 5589.
[53] K. Khan, X. Yan, Q. Yu, S.-H. Bae, J. J. White, J. Liu, T. Liu, C. Sun, J. Kim, H.-M. Cheng, Y. Wang, B. Liu, K. Amine, X. Pan, Z. Luo, *Nano Energy* **2021**, *90*, 106488.
[54] C. Cheng, S. Li, Y. Xia, L. Ma, C. Nie, C. Roth, A. Thomas, R. Haag, *Adv. Mater.* **2018**, *30*, 1802669.
[55] G. Ye, K. Zhao, Z. He, R. Huang, Y. Liu, S. Liu, *ACS Sustainable Chem. Eng.* **2018**, *6*, 15624–15633.
[56] L. Ma, S. Chen, Z. Pei, Y. Huang, G. Liang, F. Mo, Q. Yang, J. Su, Y. Gao, J. A. Zapien, C. Zhi, *ACS Nano* **2018**, *12*, 1949–1958.
[57] L. Ma, S. Chen, D. Wang, Q. Yang, F. Mo, G. Liang, N. Li, H. Zhang, J. A. Zapien, C. Zhi, *Adv. Energy Mater.* **2019**, *9*, 1803046.
[58] K. Wu, L. Zhang, Y. Yuan, L. Zhong, Z. Chen, X. Chi, H. Lu, Z. Chen, R. Zou, T. Li, C. Jiang, Y. Chen, X. Peng, J. Lu, *Adv. Mater.* **2020**, *32*, 2002292.
[59] J. Bian, X. Cheng, X. Meng, J. Wang, J. Zhou, S. Li, Y. Zhang, C. Sun, *ACS Appl. Energy Mater.* **2019**, *2*, 2296–2304.
[60] X. Chen, B. Liu, C. Zhong, Z. Liu, J. Liu, L. Ma, Y. Deng, X. Han, T. Wu, W. Hu, *Adv. Energy Mater.* **2017**, *7*, 1700779.
[61] D. Ji, L. Fan, L. Li, N. Mao, X. Qin, S. Peng, S. Ramakrishna, *Carbon* **2019**, *142*, 379–387.
[62] D. Liu, B. Wang, H. Li, S. Huang, M. Liu, J. Wang, Q. Wang, J. Zhang, Y. Zhao, *Nano Energy* **2019**, *58*, 277–283.
[63] C.-Y. Su, H. Cheng, W. Li, Z.-Q. Liu, N. Li, Z. Hou, F.-Q. Bai, H.-X. Zhang, T.-Y. Ma, *Adv. Energy Mater.* **2017**, *7*, 1602420.
[64] Z. Wang, J. Ang, B. Zhang, Y. Zhang, X. Y. D. Ma, T. Yan, J. Liu, B. Che, Y. Huang, X. Lu, *Appl. Catal. B* **2019**, *254*, 26–36.
[65] Q. Xu, H. Jiang, Y. Li, D. Liang, Y. Hu, C. Li, *Appl. Catal. B* **2019**, *256*, 117893.
[66] L. Liu, X. Zhang, F. Yan, B. Geng, C. Zhu, Y. Chen, *J. Mater. Chem. A* **2020**, *8*, 18162–18172.
[67] W. Liu, D. Zheng, L. Zhang, R. Yin, X. Xu, W. Shi, F. Wu, X. Cao, X. Lu, *Nanoscale* **2021**, *13*, 3019–3026.
[68] Y. Niu, X. Teng, S. Gong, Z. Chen, *J. Mater. Chem. A* **2020**, *8*, 13725–13734.
[69] Y. Niu, X. Teng, S. Gong, M. Xu, S.-G. Sun, Z. Chen, *Nano-Micro Lett.* **2021**, *13*, 126.
[70] J. Li, Y. Kang, W. Wei, X. Li, Z. Lei, P. Liu, *Chem. Eng. J.* **2021**, *407*, 127961.

Manuscript received: January 19, 2022
Accepted manuscript online: April 25, 2022
Version of record online: ■■, ■■

© 2022 Wiley-VCH GmbH

Research Articles

Metal–Air Batteries

T. He, Y. Chen, Q. Liu, B. Lu, X. Song,
H. Liu, M. Liu, Y.-N. Liu, Y. Zhang,*
X. Ouyang,* S. Chen* ________ **e202201007**

Theory-Guided Regulation of FeN_4 Spin State by Neighboring Cu Atoms for Enhanced Oxygen Reduction Electrocatalysis in Flexible Metal–Air Batteries

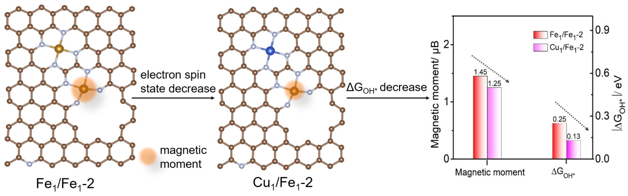

First-principles calculations show a nearly linear correlation of the energy barriers of critical oxygen reduction reaction (ORR) steps with the Fe magnetic moment of Fe-N-C composites. This is indeed observed when single Cu sites are incorporated into Fe–N–C aerogels, where the interactions between adjacent Fe–Cu 3d electrons result in a reduced magnetic moment of the Fe center and hence enhanced ORR activity.

© 2022 Wiley-VCH GmbH